

Experimental and Analytical Characterization of Firebrand Ignition of Home Insulation Materials

Savannah S. Wessies, Michael K. Chang, Kevin C. Marr and Ofodike A. Ezekoye, Department of Mechanical Engineering, The University of Texas at Austin, Austin, TX 78712, USA

Received: 20 June 2018/**Accepted:** 28 January 2019

Abstract. Wildland firebrands are known to ignite materials in attic spaces of homes. To clarify the effects of choices in attic insulation materials for homes located at the wildland urban interface, this study seeks to characterize the effects of firebrand characteristics on the ignition propensity of several common insulation materials: polyurethane foam, expanded polystyrene (EPS), extruded polystyrene (XPS), flame retarded and non-flame retarded denim, and flame retarded and non-flame retarded loosefill cellulose. An experimental system was developed to explore the effects of firebrand heating, air flow, and firebrand configuration on ignition. For an equal initial mass of wooden material, two firebrand configurations were generated: a single whole firebrand and multiple (five) fragmented firebrands. Relative to whole firebrands, the fragmented firebrands were found to more reliably ignite the insulation materials. Thermoplastic insulation material would only ignite in a temporary flash flame, but did not support sustained burning. Following the flash flame, the firebrands would melt through the synthetic polymer material (XPS and EPS) and cease smoldering. Cellulosic insulation materials would ignite in a sustained fire provided that there was adequate air flow. A simple heat and mass transfer model was developed to describe the ignition process due to firebrand deposition. Traditional lab-scale experiments, thermogravimetric analysis and cone calorimetry, were performed to parameterize the model. Results followed experimentally observed firebrand temperature patterns. There was an average error of approximately 8.5% between firebrand temperature model predictions and experimental measurements. Also, consistent with the experimental results, the model predicted that increasing air flow increased ember temperature and reduced the time to ignition for cases in which ignition occurs.

Keywords: Wildland-fire, Firebrand, Thermal insulation, Ignition-model

* Correspondence should be addressed to: Ofodike A. Ezekoye, E-mail: dezekoye@mail.utexas.edu



1. Introduction

The severity and frequency of wildland fires has been on the rise in recent years, as evidenced by the Carlton Complex Fire (2014), Anderson Creek Fire (2016), and the Thomas Fire (2017) to name just a few in the United States. Fire burns vast regions of grass and forest land area, destroys wildfire, and affects the built environment in the wildland urban interface (WUI). According to a U.S. Department of Agriculture report from 2010, 33.5% of homes in the US are in the WUI with 32.2% of the population living in these areas [1].

Assessing the potential impact of any given fire on the homes at the WUI has proven to be challenging. Wildfires are a complex coupling of meteorological factors, topography, and fuel density. Decisions on how to best protect communities at the WUI rely on predicting if and how a fire will penetrate structures. Potential fire pathways into a structure include unprotected debris laden gutters, flammable roofing materials, and firebrand transport through vents into attic spaces [2].

There is widespread agreement that vents represent a significant path for wildland fires to ignite homes [3–6]. Firebrand attack on a home's attic space leads to significant damage to the attic that can initiate further burning and structural damage to the home. To circumvent this type of home attack, communities are evaluating building codes and standard construction practices that minimize firebrand home ignition. As an example, California Building Code Chapter 7A seeks to address the access issues associated with fire into buildings through vents. Vents are a path for fire ignition either through ember transport into the vents or through direct flame impingement on the vents. Despite this awareness, there is still little understanding of the mechanisms associated with ember penetration and ignition in attic spaces. In fact, the first standardized test procedure for evaluating vent ember and flame penetration performance was not released until 2014 (ASTM E2886/E2886M). At the same time as more homes are being built at the WUI, there is growing interest in green and sustainable construction. This has expanded the variety of attic and void space insulation types that are also being used in homes. With increased frequency of wildfires and increased variability in the types of insulating materials being used in attic spaces, it is critical that careful study is conducted to understand what insulation properties make an attic space more vulnerable to wildfire threats.

Researchers have explored many potential factors affecting the ignition propensity of materials due to hot particles and/or firebrands. In regard to hot particles, there has been exploration on the relationship between the diameter and temperature of the hot particle. As an example, Wang et al. evaluated ignition properties of spherical, steel particles when deposited on low density polystyrene [7]. Hadden et al. and Urban et al. performed experiments exploring the relationship between the temperature and diameter of hot metal spheres on the ignition propensity of cellulosic fuel beds [8, 9]. Wang et al. also studied hot metal particles ignition of forest fuels with varying fuel moisture contents [10]. These studies clearly showed that probability of ignition increased with particle size. Studying ignition by hot non-reacting particles is a somewhat different problem than what occurs from hot reacting firebrands. Fewer studies of of this type of ignition (i.e., reacting parti-

cles) have been conducted. A notable example is the work of Manzello et al. [11] in which the effects of flaming versus glowing firebrands, air flow conditions, size of firebrands, and number of firebrands on the ignition of cellulosic fuels was explored. Ganteaume et al. [12] also explored the impact of air velocity and the firebrand state of reaction on the ignition of forest fuels.

Previous papers have sought to model the firebrand/hot spot ignition phenomena through various methods. Warey [13] modeled heat transfer from a firebrand to a generic substrate but did not model the reactive evolution of the firebrand and the substrate. Yin et al. [14] developed a theoretical correlation relating the time to ignition to the moisture content of a cellulosic fuel bed. Experimental data from firebrand ignition of pine needles were used to fit the correlation. Wang et al. [10] tested the ignition propensity of hot, metal spheres on cellulosic fuel beds and developed a correlation relating the experimental data on the temperature for ignition to the moisture content of the fuel and the diameter of the hot particle. These types of correlations are important to understanding experiments, however they are impractical in describing the ignition process of many materials. Experimental data would need to be collected for every material of interest. Hot spot theory is a physics based method for determining the size and temperature a hot spot needs to be to generate a self-sustaining reaction in the fuel bed. For inert hot spots, the generally preferred solution was presented by Gol'dshleger in 1972 [15]. This analysis has been employed by many different researchers to explain their results [8, 16–18]. Although this method shows some qualitative promise, many assumptions are made to apply this theory that are not necessarily true in firebrand ignition experiments. One example is the hot spot theory assumes the hot spot (firebrand) is fully embedded in the fuel, which is generally not the case, as the firebrand is deposited on the fuel bed and generally rests partially embedded on the surface. Lautenberger and Fernandez-Pello recognized the short comings of hot spot theory and proposed a combination of heat transfer and pyrolysis models and CFD analysis of the gas-phase to simulate their ignition experiments involving pine firebrands and powdered cellulose fuel beds. [19]. The complexity of this solution leads to many required inputs and the CFD component requires nontrivial computational time.

In this paper, we experimentally and analytically investigate the ignition process of various insulation materials by varying firebrand morphology and air flow speeds. The experimental procedure and results are presented in Sect. 2 for the ignition of attic insulation materials by hot reacting firebrands. Next, in Sect. 3, a simple model parameterized by insulation thermogravimetric analysis and oxygen consumption calorimetry data is presented to explain these results. The experimental data from thermogravimetric analysis and oxygen consumption calorimetry on the insulation samples are reported in Sects. 4 and 5, respectively. Using these data from traditional laboratory tests as the inputs to the firebrand ignition model, the firebrand ignition experiments are then compared to the model predictions in Sect. 6.

2. Determination of Insulation Ignition Due to Firebrands

Although the path to ignition is determined by many different factors, such as fuel moisture content, airflow conditions, chemical composition of the material, at its core, ignition is driven by a material's ability to pyrolyze at a sufficient rate to support a flame with a sufficient heat release rate to sustain the pyrolyzate production. In the case of firebrand ignition, the firebrands deposited on a substrate must transfer enough heat to the substrate to produce a sufficient rate of pyrolysis gases. The thermochemical coupling between the ember/firebrand and the substrate initiates ignition. Because the ember/firebrand smolders, there is a conversion of the chemical energy of the firebrand to thermal energy, which sustains and supports the substrate ignition. The exothermic reactions taking place in the firebrand continue to bolster the pyrolyzation and ignition of the substrate. Additional details about the physical phenomena taking place in the firebrand substrate system are discussed in later sections of this paper. The transport processes affecting an ember/firebrand on a fuel bed can be seen in Fig. 1.

Equation 1 describes the energy balance on the firebrand, where m_{FB} is the mass of the firebrand, c_{FB} is the specific heat of the firebrand, \dot{Q}_{rxn} is the heat generated by exothermic reactions, \dot{Q}_{rad} is the radiative heat loss, \dot{Q}_{cond} is the heat lost by the firebrand to the fuel bed due to conduction and radiation, and \dot{Q}_{conv} is the convective heat loss from the firebrand. In order to fully describe this system, meaningful coupling between the firebrand properties and ignition characteristics of the substrate is needed. There is a dependence on the substrate's thermophysical and kinetic properties that needs to be more fully detailed.

$$m_{FB}c_{FB} \frac{dT}{dt} = \dot{Q}_{rxn} - \dot{Q}_{rad} - \dot{Q}_{cond} - \dot{Q}_{conv} \quad (1)$$

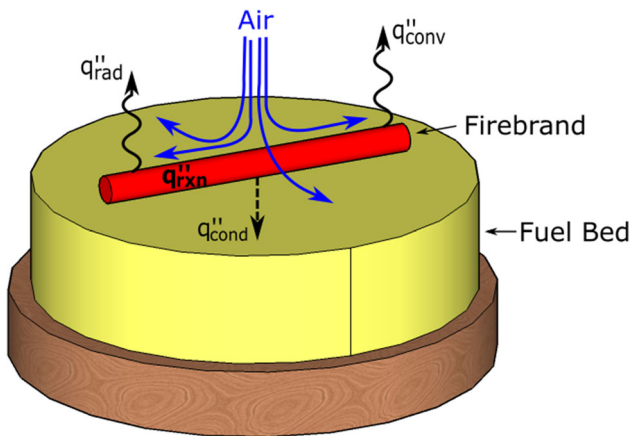


Figure 1. Heat transfer processes around a firebrand deposited on a solid fuel bed.

To inform the model prediction of ignition, various experiments must be conducted. At the highest level, there is a need for observational results and measurements of ignition for different types of insulation materials and ember configurations. Beyond this, we will show that the use of small scale tests informs model predictions of these high level ignition tests.

2.1. Experimental System and Test Procedure

The experimental system shown in Fig. 2 was developed to heat firebrand samples to a desired reactive condition before deposition onto a fuel bed. The heating process occurred in a Thermolyne Model F21115 tube furnace. Firebrands were created by sectioning commercially available 10 mm diameter pine dowels, drying them in an oven at 105°C, and heating them in the furnace for a prescribed time. It was found that drying the dowels reduced the likelihood of generating fractured firebrands in the high temperature processing and improved the overall repeatability of the firebrand production process. Two firebrand morphologies were investigated—a large firebrand and a small pile of fragmented firebrands. The large and fragmented firebrands have the same initial mass of 0.4 g and were created using a single 50-mm long section and five 10-mm long sections, respectively.

The firebrands were placed inside of a mesh basket suspended centerline in a 420°C furnace for approximately 200 s. Single, large firebrands and fragmented firebrands were both placed in the mesh basket within the furnace at the same height to ensure there were no differences in the heating process. These conditions

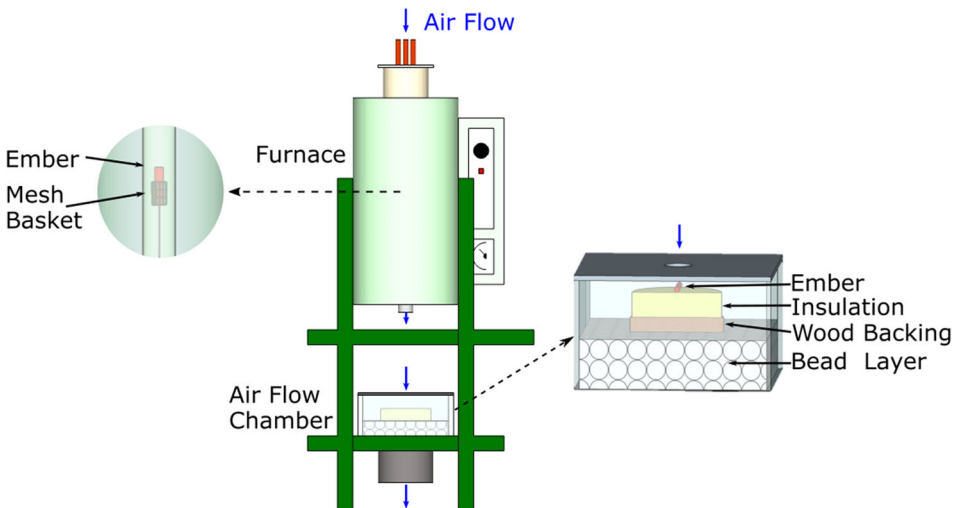


Figure 2. Schematic of firebrand ignition test setup. Arrows show air flow direction. Left side close up shows the ember placement in furnace for heating. Right side close up features the placements of the sample and firebrand within the air flow chamber.

produced glowing firebrands and reduced the diameter to approximately 6.0 ± 0.34 mm. Additionally, the mass of the exiting firebrands was reduced to 0.31 ± 0.077 g for the large firebrands and 0.20 ± 0.029 g for the fragmented firebrands. The diameter of the exiting firebrands was found by first quenching the reacting firebrand in nitrogen and then measuring the diameter. This firebrand diameter was chosen for two reasons: first, the firebrand size should be within the range of naturally occurring firebrand dimensions, and second, the firebrand should be able to fit through an attic vent. Based on experimental work by Manzello et al, firebrands generated from wildland vegetation varied in size from 0.5 mm to 15 mm in diameter and 1 mm to 425 mm in length [20]. In that same paper, they found conditions in which they measured an average firebrand size of 5 mm in diameter and 34 mm in length. El Houssami et al. collected 330 firebrands from wildland vegetation that ranged in thickness from 1 mm to 6 mm [21]. Based on these data, the firebrands from this study are within a size range that could be produced naturally. The 2018 International Residential Code for One and Two Family Dwellings, Section R806.1 states that attic ventilation should have openings between 1.6 mm and 6.4 mm. The firebrands produced in this project are nominally 6 mm in diameter and could penetrate code-approved attic ventilation screens [22].

The tube furnace used in these experiments had an outer diameter of 42.5 mm and inner diameter of 35.5 mm. Due to the diameter of the tube furnace, there was a thermal gradient in the radial direction. The thermal gradient was measured using a series of thermocouples at different radial positions. In order to reduce this gradient, mixing of the gases within the furnace was induced by flowing 10.4 L/min of air through three copper tubes at the top of the furnace and reducing the opening at the bottom to restrict the outflow of air. This adjustment reduced the thermal difference across the furnace tube section from 80°C to approximately 10°C.

After a symmetric, glowing ember without observable cracks was produced, it was placed on the fuel bed inside the air flow chamber. Firebrands were deposited on the substrate through a 2.5 cm opening centered above the fuel bed. The air flow chamber consisted of a plenum with a machined hole on top and 5.75 mm diameter beads used as flow conditioning elements at the bottom of the plenum. Air flow was induced through the plenum using a 0.93 kW electric vacuum. The flow rate of the air was controlled varying the voltage supplied to the vacuum with a variac. Three different air flow conditions were tested—natural convection and two induced flows, 2 m/s and 9 m/s. These velocities were measured at the inlet of the plenum using a pitot-static probe. Nominally, the air flow onto the firebrand resembled a stagnation point flow. The insulation sample was placed atop a piece of plywood to simulate typical boundary conditions in an attic. The wood and insulation bed were centered on the flow conditioning elements in the plenum.

During the large firebrand tests, the firebrand was deposited horizontally on the insulation sample. In the fragmented case, a mesh tube was used to deposit the firebrands onto the insulation bed to ensure that the firebrands remained on the sample during testing. Unlike the large firebrand which always rests horizontally

on the substrate, the placement of the fragmented firebrands is somewhat random. The fragmented firebrands tend to stack on one another, but over the course of many tests, the base area of the pile remained constant in a roughly circular pattern. The insulation sample was instrumented with three 24 gauge, braided fiber-glass Type-K thermocouples embedded in various locations approximately 1-2 cm from the firebrand. The thermocouples were offset from the firebrand to minimize intrusion errors. A schematic of the thermocouple placement can be seen in Fig. 3. Additionally one of the walls of the plenum was made of an IR transmissive material allowing for the tests to be observed with an FLIR e40 IR camera. The temperature of the firebrand was taken to be the maximum temperature in the range of interest in the IR image.

In order to use the IR camera to collect temperature data from the firebrands, the emissivity of the firebrand is required. A simple calibration procedure was

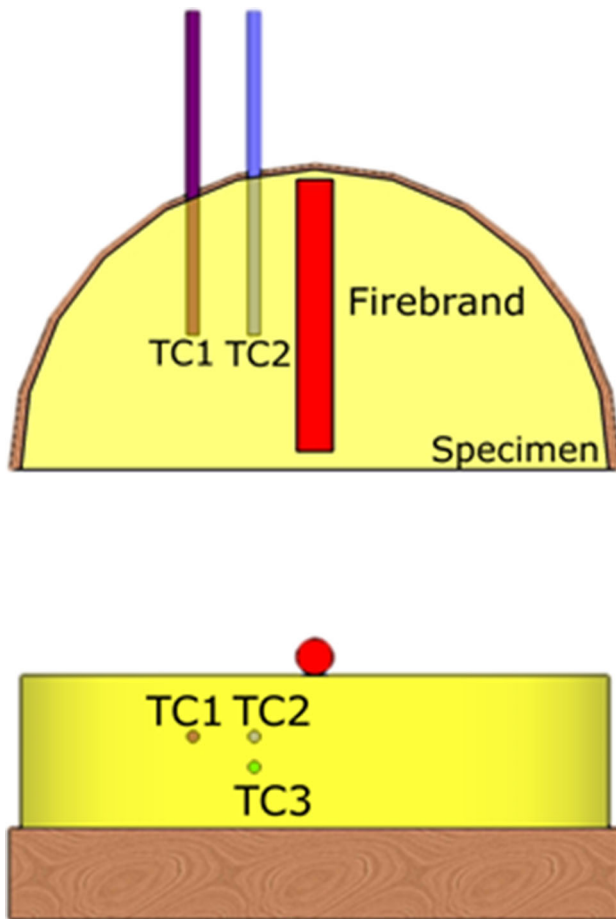


Figure 3. Top and front view of the thermocouple placement in the insulation sample.

employed to measure the firebrand emissivity. A firebrand was generated in the same method detailed above using the furnace. At a sufficiently high temperature, the firebrand was removed from the furnace and inserted into a nitrogen gas environment to quench reactions. This produces a firebrand with the same surface properties as the firebrands used in the ignition experiments. Using the IR camera, the firebrand was heated, and the temperature was compared against a known value. Using this procedure, the firebrand emissivity was found to be 0.8.

Five different types of commercially available flame retarded insulations were tested—Ultratouch denim, Greenfiber loose-fill cellulose, Dow Great Stuff Big Gap Filler Polyurethane spray foam (PUR), Owens Corning FOAMULAR 250 extruded polystyrene (XPS), and Cellofoam Poly Panel expanded polystyrene (EPS). Based on the manufacturer's technical data sheets, the thermal conductivities of these materials ranged from 0.022 W/mK to 0.46 W/mK, with XPS having the lowest and cellulose having the highest. The specific heat capacities for the materials were between 1300 J/kgK and 1500 J/kgK, and the densities ranged from 20 kg/m³ to 50 kg/m³. In order to explore the effects of flame retardants (FR), non-flame retarded (NFR) denim and cellulose were also tested. To further categorize the insulation materials, they can be separated into cellulosic (denim and cellulose, both FR and NFR) and synthetic polymeric (PUR, XPS, EPS) materials. All materials had, at a minimum, triplicate tests performed for every combination of the three flow conditions and the two firebrand morphologies.

2.2. Results

Ember deposition on the fuel bed resulted in four observable outcomes—extinction, smoldering ignition, flash flaming ignition, and flaming (sustained) ignition. Characteristically, flash flames are wisps of fire that only last for a few seconds, and the fuel bed remains relatively unchanged. Visually, there is a characteristic flickering of small flames in flash flaming. In contrast to sustained ignition, where flames grow and spread across the substrate, flash flames have a short residence time and don't propagate across the fuel bed in the same way. A photo progression of flash flaming can be seen in Fig. 4. Upon contact with the firebrands, the PUR begins to degrade slightly. This can be observed by the firebrands sinking into the fuel bed. At 13 s, small initial flames can be seen around in firebrand pile. A flame can be seen above the fuel bed at 15 s. By 17 s, the flames have extinguished. These flames only lasted for a few seconds before extinguishing. This definition of flash flaming is in contrast to Wang et al., who defined ignition as a flame of at least 1 s [10]. By classifying shorter, transitory flames as flash flames and longer, sustained flames as an ignition event, materials can be divided into more descriptive categories. Materials that exhibit flash flames may be more likely to self-extinguish compared to materials where sustained flaming occurred. It is important to note that the flaming observed in these tests was from the substrate and not the firebrand. Separate tests were conducted with the reacting firebrand on inert substrates. The same method was used to produce the firebrands and test the substrate, however with an inert substrate, flaming ignition did not occur. The process in which the firebrands are produced helps ensure that flaming ignition of

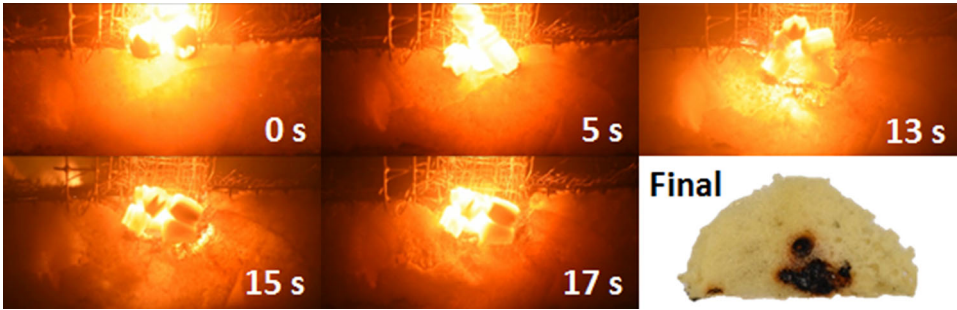


Figure 4. Photo progression of flash flaming for fragmented firebrands on PUR with an induced flow of 2 m/s.

the firebrand does not occur after leaving the furnace. After an initial heating period within the furnace, flaming ignition is observed on the firebrand. While the firebrand is still contained within the furnace, the flames will engulf the firebrand and after a time, extinguish. The gas phase extinction process is an indication that volatiles within the firebrand are essentially consumed. This process produces a firebrand that would not reignite under a variety airflow conditions when deposited on various inert substrates, and even when a flame was directly applied to the firebrand.

Table 1 shows the results of the firebrand ignition tests for the various insulations for the two induced flow conditions and the two firebrand morphologies. For all of the natural convection cases, the firebrands extinguished without ignition of the fuel bed. This occurred for both the large and fragmented firebrands.

Table 1 Results for Firebrand Ignition Tests

Material	Firebrand	2 m/s Air flow	9 m/s Air flow
Denim	Large	TTI = 35 s (7 s, 63 s)	TTI = 7 s (4.6 s, 9.4 s)
	Fragmented	TTI = 17.8 s (10.7 s, 24.9 s)	TTI = 4 s (2 s, 6 s)
NFR denim	Large	TTI = 37.7 s (15.4 s, 60 s)	TTI = 9.3 s (5.2 s, 13.4 s)
	Fragmented	TTI = 4 s (2.3 s, 5.7 s)	TTI = 2.8 s (1.5 s, 4.1 s)
Cellulose	Large	Flash flaming	TTI = 13.5 s (0 s, 30.2 s)
	Fragmented	Flash flaming	TTI = 18.6 s (2.6 s, 34.6 s)
NFR cellulose	Large	TTI = 4.6 s (2.7 s, 6.5 s)	TTI = 4.3 s (3.7 s, 4.9 s)
	Fragmented	TTI = 4 s (2.2 s, 5.8 s)	TTI = 1.4 s (0.7 s, 2.1 s)
PUR	Large	Flash flaming	Flash flaming
	Fragmented	No ignition	Flash flaming
XPS	Large	No ignition	Flash flaming
	Fragmented	Flash flaming	Flash flaming
EPS	Large	No ignition	Flash flaming
	Fragmented	Flash flaming	Flash flaming

If sustained, flaming ignition occurred, the average time to ignition(TTI) is listed with the confidence interval in parentheses

The behavior was found to be consistent across the triplicate tests for each condition. Some FR insulations displayed more variability in ignition times compared to other materials, specifically cellulose. This might be attributed to an inconsistent flame retardant loading. In the case of the synthetic polymeric insulations, the flame retardants were added to the mix before being formed allowing for a consistent flame retardant loading. For the cellulosic materials (i.e., recycled newspaper), the application of FR chemicals occurs in a macroscale mixing process that likely has microscale variability. Several of the insulations exhibited some flash flaming. Upon firebrand deposition, the synthetic polymeric insulations would melt. Flash flames would typically occur after several seconds as the firebrands begin to melt through the polymer. The flash flames burn for several more seconds before extinguishing. In the cases of XPS and EPS particularly, the firebrands would melt through the insulation until they reached the wood backing. A large cavity formed in the insulation above the firebrand after it had melted through the insulation. Once the firebrand was completely subsumed within the polymer, re-ignition was not observed. Above the cavity region created by the hot firebrand, where the pyrolyzed gas and air mixture is flammable, no pilot exists. In the cavity where a pilot in the form of the hot firebrand exists, the ratio of fuel to air is likely greater than the upper flammability limit. In cellulose and PUR, the time to flash flaming was generally longer than for XPS and EPS.

At lower inlet air velocities, the oxidation rate of the firebrand is relatively small, allowing ash layer growth and the heat losses to the environment and insulation to cool the firebrand. Under these conditions, minimal insulation degradation occurs and flaming is not observed. At higher inlet air velocities, the oxidation rate of the ember increases, generating sufficient heat to overcome the losses to the insulation and the environment. As the fuel bed temperature rises, the rate of pyrolysis increases until a flammable fuel–air mixture is reached.

As such, the tests showed that a non-zero air flow rate was necessary for ignition. This suggests that there is a critical rate of the firebrand's oxidative reaction required for ignition. Fourteen of the forty-two conditions had flaming ignition, FR and NFR denim and NFR cellulose at 2 m/s and 9 m/s and FR cellulose at 9 m/s with both firebrand types (Table 1). Consistent with previous work by Damant et al. who investigated cigarette ignition of upholstered furniture, synthetic polymers were less prone to flaming ignition than cellulosic fibers [23]. Pre and post-test comparisons of the different fuel beds with both firebrand types can be seen in Fig. 5.

The imprints left in the single large firebrand tests can be seen in column two and three of Fig. 5, as compared to the more circular damage region from the fragmented firebrand tests shown in column four and five. From these post test images, the differences between the charring polymer systems and the melting systems are more obvious. For instance, the polystyrenes, XPS and EPS, melted when the firebrands made contact forming large cavities. The melted material also formed a tar like black substance that can be seen most clearly in the XPS pictures. For the PUR cases, the majority of the material is unchanged. The flash flaming did not propagate through the material, and a clear char region can be seen where the firebrand made contact with the substrate. Additionally, another

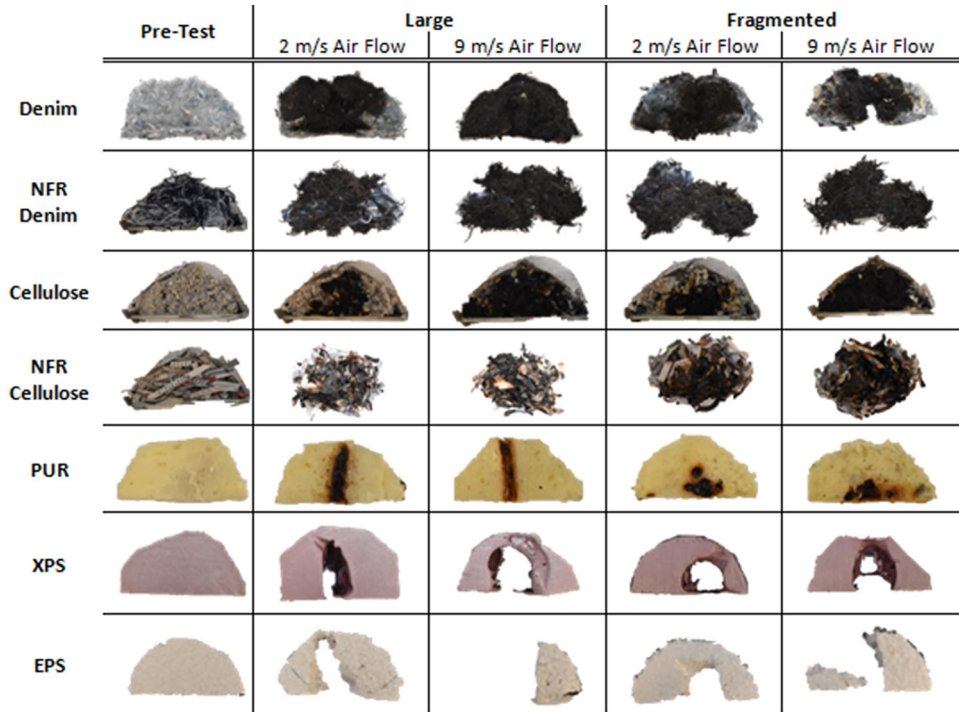


Figure 5. Insulation samples before and after firebrand ignition tests.

region that is lighter than the char can be seen, where the material began to degrade and pyrolyze, but there was no smoldering or flaming combustion. It is also clear that there is a difference in the amount of fuel bed damage between the flash flaming and sustained ignition materials. For the cellulosic materials, which experienced sustained ignition, it is clear that the flames propagated across the majority of the material surface through the charring and degradation visible in the images. However for the synthetic polymers that experienced flash flaming the damage is localized to regions near the firebrand. The effects of increased airflow are visible through the increased damage to the substrate for the 9 m/s air flow cases compared to the 2 m/s cases. A comparison of the time to ignition (TTI) for FR and NFR cellulosic materials is shown in Table 1. From these results, the effects of the flame retardants are not entirely obvious. However, the effects of changing the firebrand morphology and air flow conditions were more concrete. In general, the fragmented firebrands had quicker ignition times compared to the large firebrands. Additionally, as the air flow rate increased, the ignition times decreased.

The times to ignition were calculated by averaging at least five tests for each test condition. If a sustained ignition event occurred during the initial triplicate,

additional tests were conducted. As mentioned, in general, the fragmented firebrands had faster ignition times. The surface area in contact with the fuel bed for the fragmented firebrands was approximately 25% less than that for the large firebrand as estimated by image analysis of the char left by the different firebrand configurations on PUR in non-ignition cases. This area difference is because the fragmented firebrands can form a pile and rest on one another. Although the contact area was less in the fragmented firebrand cases, the surface area exposed to air was larger in the fragmented cases versus the large, whole firebrand. The oxidation rates increase with increasing surface area, leading the fragmented firebrand to have higher oxidation rates compared to the large firebrand. Additionally, the heat loss from the bottom-most firebrands to the ambient environment for a pile of fragmented firebrands was less than that of a single large ember. The fragmented firebrands radiate to one another, helping maintain higher temperatures for longer periods of time compared to the large firebrand. Using IR measurements, it was shown that the cooling time from 600°C to 300°C for a large firebrand placed on an aluminum substrate was half the time of fragmented firebrands cooling time over the same temperature range. Although the aluminum substrate leads to different firebrand temperatures and cooling times, this test demonstrates that the heat transfer mechanisms differ between fragmented and whole firebrands. Combined, the increased surface oxidation area and reduced radiative losses resulted in higher heat fluxes from the fragmented embers to the substrates, leading to higher insulation pyrolysis rates and shorter TTIs.

The confidence intervals shown in Table 1 were calculated using a 95% confidence interval Student's t-distribution and represent the variability from test to test. For the fragmented firebrands, the TTIs ranged between 2 s and 36 s. The large firebrand cases had a larger spread from 2 s to 63 s. One significant source of uncertainty is the variability between tests samples which may include non-uniformity of FR loading, local density, and material characteristics. The NFR cases with higher air flow conditions exhibit less uncertainty. Significant uncertainty was observed in the large firebrand tests for FR and NFR denim at 2 m/s, the fragmented firebrand test for FR denim at 2 m/s, and the large and fragmented firebrand tests for cellulose at 9 m/s. The source of the uncertainty is likely the result of these cases approaching the critical heat flux for ignition. In this regime, TTI is more sensitive to variability in the test conditions and material. At higher air flows, the uncertainty decreases due to an increase in the oxidation rate, resulting in higher firebrand temperatures. As the temperature of the firebrand increases, the heat flux from the firebrand to the substrate increases and can eventually exceed a critical heat flux. The overall variability and stochasticity of ignition events would suggest that exceeding the distribution of critical heat flux values by a ever widening amount would lead to more reliable ignition events. This is consistent with Zak reporting that the probability of a stainless steel sphere igniting alpha-cellulose dropped from 95% to 5% when the temperature of the sphere was reduced from 670°C to 610°C [24].

Figure 6 shows the temperature for the thermocouples embedded in the insulation and the IR camera derived firebrand temperature during testing of FR denim at 9 m/s. This case resulted in ignition at approximately 5 s. All cases where igni-

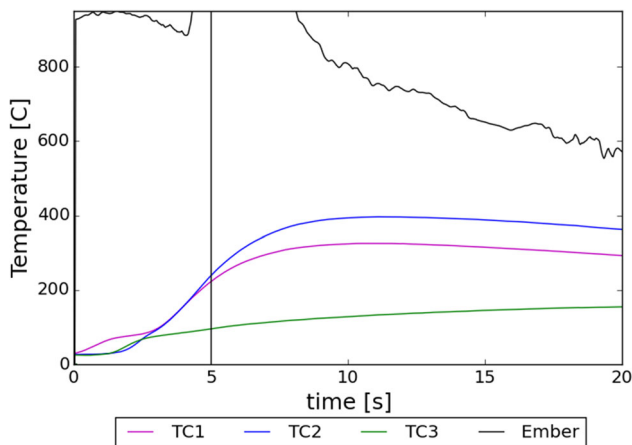


Figure 6. Large firebrand ignition of FR denim (9 m/s) with vertical line indicating TTI.

tion occurred showed heavy smoke production, a sharp increase in fuel bed temperature, and a bright glowing firebrand. Recall that the thermocouples are offset from the location of the firebrand, so there is a slight delay in the thermocouple readings. During ignition, the luminosity of the flames saturates the range of the IR camera. Once the flame moves away from the firebrand, the derived IR temperature is again recovered. Similar characterization was conducted for all materials. From these thermal characterizations of the fuel beds, we can infer how heat is transported through the material. For the case seen in Fig. 6, the two thermocouples (TC 1 and 2) nearer to the surface of the fuel bed had much higher temperatures when compared to TC 3, which was embedded deeper in the material. From the spatial distributions in measured temperatures, it seems that the denim material more readily transfers heat in the lateral direction compared to the vertical direction.

A photo progression of the IR images from Fig. 6 can be seen in Figure 7. In the upper left image ($t = 0$), the firebrand is initially deposited on the fuel bed. As time progresses, the area surrounding the firebrand begins to warm up and the firebrand itself increases in temperature. Ignition in this test occurred at 5 s; in this frame, the temperature of the firebrand reaches the maximum of the measurable range. In the following two frames presented, 6 s and 7 s, the area of increased temperature expands. The firebrand is sufficiently high that the IR camera measured temperature saturates. The final frame ($t = 20$ s) is after flame extinguishment and the substrate and firebrand have both begun to cool. The temperatures in this frame are much lower than those seen previously in the test. It is interesting to compare these IR images where ignition occurs relatively quickly to a test where ignition occurs at a much later time. Figure 8 shows an IR photo progression of a large firebrand on denim at 2 m/s. In this particular test, ignition occurs well after the 20 s presented. It is important to note that the time stamps are not the same as those in Fig. 7. Comparing the two figures, it is clear

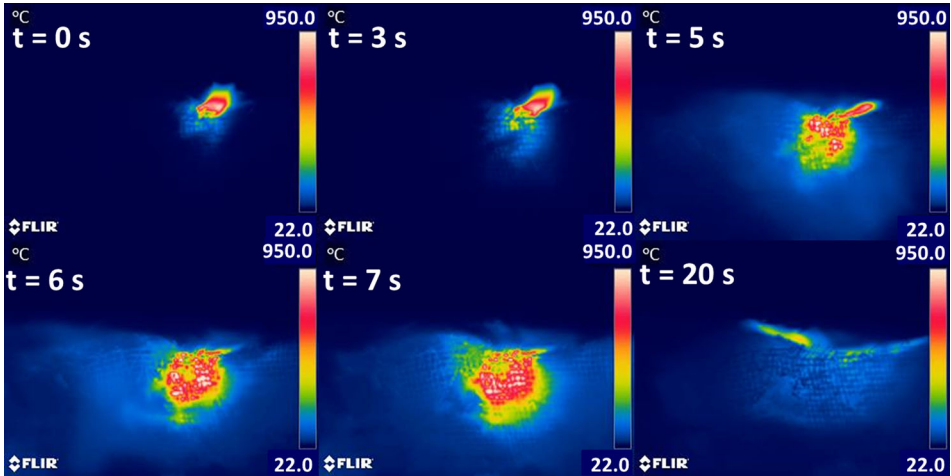


Figure 7. IR photo progression of the large firebrand ignition of FR denim (9 m/s). The IR frames presented match the test presented in Fig. 6.

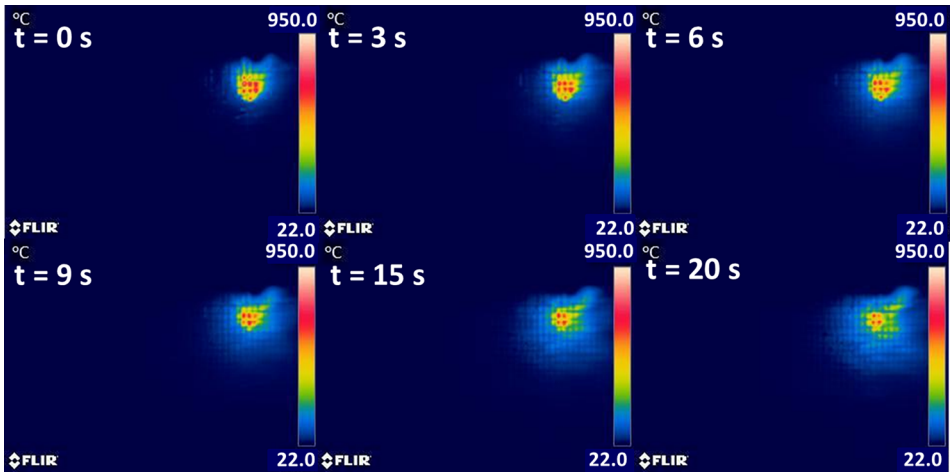


Figure 8. IR photo progression of the large firebrand deposition on FR denim (2 m/s). Ignition does not occur during this time frame.

that the temperature of the firebrand in the 2 m/s flow is much lower than temperatures experienced in the 9 m/s. Also the temperature is localized in the 2 m/s case compared to the 9 m/s case.

3. Analytical Model of Firebrand Ignition

Because firebrand ignition of fuels is a complex process depending on many parameters, such as the air flow rate, the reactivity of the firebrand, and the thermophysical properties of the fuel, there is value in developing a simple analytical tool to explain the ignition processes. Our model seeks to explain the firebrand ignition process through a simple heat and mass transfer analysis. There are three basic elements to the model/analysis. These are:

1. Prediction of the firebrand temperature evolution
2. Prediction of the specimen temperature and mass flux of pyrolysis gases from the specimen
3. Development of an ignition criterion for the firebrand-specimen system

The model and the ignition criterion will be matched to the experimental results from the firebrand ignition experiments and parameterized by two traditional bench scale tests—thermogravimetric analysis (TGA) and oxygen consumption calorimetry via a cone calorimeter.

3.1. Prediction of the Firebrand Temperature Evolution

An energy balance for the firebrand was presented in Eq. 1. Balancing the smoldering source term with the radiative and convective losses to the environment yields Eq. 2.

$$\dot{m}''_{ox} \Delta H_{ox} = \left(\frac{Y_{ox,\infty} \Delta H_{ox}}{\frac{1}{h_m} + \frac{\gamma}{\rho D}} \right) = q''_{RAD,FB-\infty} + h(T_{FB} - T_{\infty}) \tag{2}$$

There are two parts to the transport resistance between the freestream oxygen mass fraction and the reactive sink. One is defined in terms of h_m which is the standard mass transfer coefficient and the other is defined in terms of a diffusive resistance through the consumed parts of the firebrand. Essentially, it is postulated that as the firebrand is oxidized, a porous ash layer grows on the firebrand and inhibits oxygen diffusion. The thickness of the layer is called γ . The mass transfer coefficient can be modeled as h/c_p , where c_p is the specific heat capacity. The other terms in this equation are \dot{m}''_{ox} , which is the mass flux in terms of the oxygen, ΔH_{ox} is the heat of combustion on an oxygen basis, $Y_{ox,\infty}$ is the ambient mass fraction of oxygen, ρ_{FB} is the gas density, D is the mass diffusivity of the oxygen, $q''_{RAD,FB-\infty}$ is the heat flux due to radiation from the firebrand to the environment, h is the heat transfer coefficient, T_{FB} is the temperature of the firebrand, and T_{∞} is the ambient temperature.

Radiation is modeled as a two surface enclosure, as seen in Eq. 3.

$$q''_{RAD,FB-\infty} = \frac{\sigma(T_{FB}^4 - T_{\infty}^4)}{\frac{1-\epsilon_{FB}}{\epsilon_{FB}A_{FB}} + \frac{1}{F_{FB-\infty}A} + \frac{1-\epsilon_{\infty}}{\epsilon_{\infty}A_{\infty}}} \tag{3}$$

In modeling the firebrands, we assume that the view factor from the underside of a single large firebrand to the substrate surface, $F_{FB-\infty}$ is unity. This differs from the the view factor for a pile of fragmented embers that radiatively “see” each other. For this pile of embers/firebrands, we approximate them to be a hemispherical pile and the view factor from the inner surface of the hemisphere to the substrate is 0.75. In Eq. 3, ε_{FB} is the emissivity of the firebrand.

Equation 2 can be rewritten as:

$$\left(\frac{Y_{ox,\infty} \Delta H_{ox}}{\frac{1}{h_m} + \frac{\gamma}{\rho D}} \right) - (\varepsilon_{FB} \sigma F_{FB-\infty} (T_{FB}^4 - T_{\infty}^4) + h(T_{FB} - T_{\infty})) = 0 \quad (4)$$

The ash layer thickness, γ , can be modeled as a time dependent function that depends on the mass loss rate of the firebrand due to smoldering. For a smoldering reaction assumed to be:



The rate of carbon mass loss is given by:

$$\frac{dm_{FB}}{dt} = -\rho_{FB} 2\pi R_o l \frac{d\gamma}{dt} = -2\pi R_o l \dot{m}_c'' = -2\pi R_o l \left(\frac{Y_{ox,\infty}}{\frac{1}{h_m} + \frac{\gamma}{\rho D}} \right) \frac{v_c W_c}{v_{ox} W_{ox}} \quad (6)$$

Note that v_{ox} and v_c are the stoichiometric coefficients of oxygen and carbon in the reaction. W_{ox} and W_c are the molecular weights of oxygen and carbon. R_o is the nominal radius of the firebrand, and l is the length of the firebrand.

Thus, the ash layer thickness can be specified as:

$$\rho_{FB} \frac{d\gamma}{dt} = \left(\frac{Y_{ox,\infty}}{\frac{1}{h_m} + \frac{\gamma}{\rho D}} \right) \frac{v_c W_c}{v_{ox} W_{ox}} = \Gamma \left(\frac{Y_{ox,\infty}}{\frac{1}{h_m} + \frac{\gamma}{\rho D}} \right) \quad (7)$$

After separation and integration, it is easy to show that the ash layer thickness evolves as:

$$\left(\frac{\gamma}{R_o} \right) = \left[\left(\frac{\rho D}{h_m R_o} \right)^2 + \left(2 \frac{\rho D}{R_o} \frac{t}{\rho_{FB} R_o} \Gamma Y_{ox,\infty} \right) \right]^{1/2} - \left(\frac{\rho D}{h_m R_o} \right) \quad (8)$$

The fact that γ grows in time means that the overall resistance to oxygen transport grows in time and that the firebrand/ember cools with increasing time, which is consistent with experimental observations.

The velocity from the firebrand ignition experiments is defined at the orifice to the airflow chamber for each scenario. The airflow conditions will be modeled as a stagnation point flow. Based upon the Reynolds number at the orifice, a correla-

tion from Persoons et al. was used for the Nusselt number correlation [25]. Their Nusselt number for stagnation point flows is seen in Eq. 9.

$$Nu_{D,o} = \frac{hD_{ORF}}{k} = 0.585Re_{D,o}^{0.5}Pr^{0.4} \quad (9)$$

In the above equation, k is the gas thermal conductivity, D_{ORF} is the orifice diameter, Pr is the Prandtl number, and $Re_{D,o}$ is the Reynolds number based upon the orifice diameter. The velocities used to calculate the Reynolds number were 0.1 m/s, 2 m/s, and 9 m/s to represent natural convection and the two induced flow cases. The heat transfer coefficient calculated for natural convection using the 0.1 m/s velocity and Eq. 9 matched well with the results from a correlation for the free convection on a heated horizontal plate [26]. For the firebrand radiation temperature calculation, the emissivity is assumed to be 0.8, as measured in the firebrand ignition experiments, and the specimen (fuel) is initially taken to be at the same temperature as the surroundings. The specific heat capacity of the oxidizer is taken as $1040 \frac{J}{kgK}$ [26]. The heat of combustion on an oxygen basis is taken to be $\Delta H_{ox} = 13.59 \text{ MJ/kgO}_2$ [27]. The mass fraction of oxygen in the free stream is $Y_{\infty} = 0.23$. The firebrand temperatures are solved for iteratively using a simple Newton method.

3.1.1. Firebrand Temperatures from Model and Experiments Table 2 shows the IR measured firebrand temperature from the firebrand ignition experiments for the various air flow conditions and the two different firebrand morphologies and the model predicted firebrand temperatures for the various experimental configurations. These firebrand temperatures are taken at the deposition time for the experimental cases and the initial value predicted by the model. The experimental temperatures are measured using IR imagery, which is dependent on the the emissivity of the item. The emissivity of the firebrand is 0.8, as measured in the firebrand ignition experiments. Sensitivity analysis was performed on the measured firebrand temperature to quantify the uncertainty due to the chosen emissivity value. The emissivity of the firebrand was perturbed 5% in either direction for the IR data collected for each case. This led to approximately 1% to 3% difference in temperature measurements when compared to the 0.8 emissivity temperatures. In both the experiments and the model, the firebrand temperature increases with increasing air flow. Additionally, the fragmented firebrands have higher temperature than the large firebrand in each air flow condition for both the experimental and model results. The maximum percentage error in the firebrand temperature predictions is 19% and occurs for the natural convection on large firebrand case. The minimum percentage error is 2% and occurs for the 2 m/s large ember case. In general, the temperature trends are the same between the model predictions and experimental results with average temperature error for these cases of approximately 8.5%.

The temperature of the firebrands, both large and fragmented, vary with time. Figure 9 shows model predicted temporal variation in firebrand temperature com-

Table 2
Comparison of Experimentally Determined Firebrand Temperature and Model Predicted Firebrand Temperature

	Natural convection	2 m/s Air flow	9 m/s Air flow
Large T_{FB}	600 K/737 K	1056 K/1033 K	1097 K/1216 K
Fragmented T_{FB}	874 K/787 K	1149 K/1101 K	1235 K/1293 K

Temperatures are displayed as experimental/model

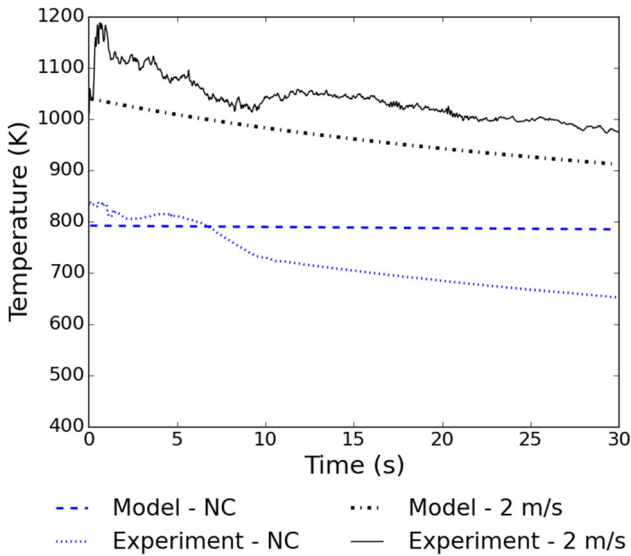


Figure 9. Comparison of the model and experimental firebrand temperatures. The natural convection (NC) data presented is for the fragmented firebrand configuration. The data presented for the 2 m/s case is for the large firebrand configuration.

pared against the IR measured firebrand temperature from two different insulation ignition tests. The experimental data presented are from a large firebrand deposited on denim with the 2 m/s air flow condition and fragmented firebrands deposited on cellulose under a natural convection condition. It is important to note that the model temperature is only valid before ignition occurs. In the natural convection case, there was no ignition. The time to ignition in the 2 m/s case was much longer than the time period shown in Fig. 9. The overall trend in the firebrand temperature and the magnitude matches fairly well for the 2 m/s case. For the natural convection case, the experimental temperature cools more quickly initially compared to the model.

3.2. Prediction of the Specimen Temperature and Mass Flux of Pyrolysis Gases from the Specimen

Given the temperature evolution model of the firebrand, there is an associated fuel mass flux produced by this high temperature ember/firebrand. One way to decouple the process is by defining a radiative coupling. Radiative coupling, for this purpose, refers to the radiative thermal exchange between the ember and the substrate. Both of these objects have rough exteriors, leading to very small points of contact. The majority of the heat transfer between the two surfaces will be due to radiation, rather than conduction, as the contact area is small and the contact resistance is high. To first order, we assume that a radiative flux exists between the firebrand and the specimen/insulation

We expect the specimen temperature to increase from the heat flux from the firebrand. This radiative heat flux causes conduction into the insulation material, pyrolysis of the substrate, and induces convective cooling of the substrate as shown in Eq. 10. In this equation, L is the heat of pyrolysis.

$$q''_{RAD} = \dot{m}''L + q''_{COND} + q''_{CONV} \tag{10}$$

The mass loss is modeled using an Arrhenius model, Eq. 11, for the insulation which is informed by cone calorimetry and TGA data. We model \dot{m}''_o as an asymptotic burning mass flux that is identified by cone calorimetry. The activation energy, E , and pre-exponential factor, A , are derived from TGA measurements.

$$\dot{m} = \dot{m}''_o A e^{-E/(RT_{INS})} \tag{11}$$

Conduction into the specimen is modeled using a temporally evolving simple diffusion thickness model, based on the concept of a thermal penetration depth into a semi-infinite solid. The thermal penetration depth is $\delta \approx \sqrt{\alpha t}$, and we approximate the gradient in Fourier’s law by the temperature difference between the substrate and the initial temperature divided by $\delta(t)$. Putting together these relatively simple model forms yields the insulation specimen temperature equation:

$$\sigma(T_{FB}^4 - T_{INS}^4) = \dot{m}''_o A e^{-E/(RT_{INS})} L + \left(h_{NC} + \sqrt{\frac{k_{INS} \rho c_p}{t}} \right) (T_{INS} - T_o) \tag{12}$$

At each time, the insulation temperature is solved using a simple Newton root finding method.

3.2.1. Specimen Temperatures from Model At early times, the incident heat flux from radiation is essentially balanced by conductive losses and the temperatures are relatively low. At much later times, the radiative transfer balances the flux production. Note, however, that at these later times the heat transfer into the specimen is relatively small because the surface (specimen) temperature begins to approach the source (firebrand) temperature. Figure 10 shows the temperature

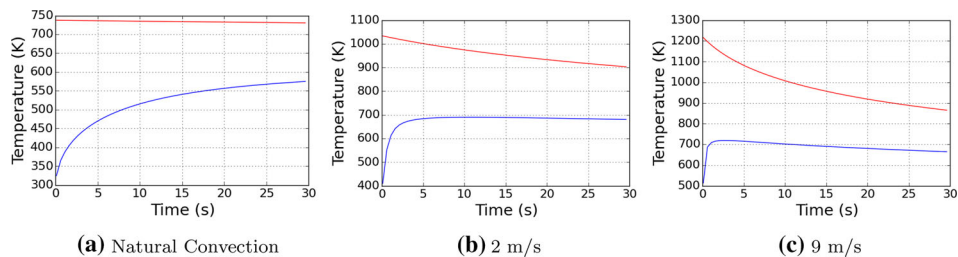


Figure 10. Specimen temperature over time for a large ember on a representative substrate for the experimental air flow conditions. The red line indicates the firebrand temperature and the blue line represents the specimen temperature.

evolution for the firebrand and specimen under natural convection, 2 m/s air flow, and 9 m/s air flow cases, respectively. These figures represent a large ember on a substrate with the following kinetic parameters: $E = 100 \text{ kJ/mol}$ and $A = 4e6 \text{ s}^{-1}$. These values are for a representative case and do not match a specific insulation from the tests. Comparing the natural convection case to the two induced flows (2 m/s and 9 m/s) shows that the increased air flow leads to higher firebrand and specimen temperatures and a faster increase in specimen temperature.

3.2.2. Specimen Mass Fluxes from Model The mass flux of pyrolysis gases from the specimen is dependent on the kinetic parameters of the specimen and the specimen temperature. The specimen temperatures from Eq. 12 are used to predict the mass flux of pyrolysis gases using Eq. 11. The mass flux over time for the representative cases can be seen in Fig. 11. It is assumed that the decomposition kinetics of the substrate material prescribe the rate of pyrolysis production for the affected area. The mass loss rate is defined per unit area of the heat affected region. As such, one can readily compare mass loss rates per unit area with cone calorimeter based results.

3.3. Development of an Ignition Criterion for the Firebrand-Specimen System

In 1946, Bamford et al. presented the rate of the production of fuel vapors from combustible solids as an ignition criterion [28]. They proposed a minimum critical rate of fuel vapor for production based on wood ignition experiments. Since the introduction of this criterion, many researchers have performed experiments and developed theoretical models to explore the validity of the critical mass flux criterion for ignition [29, 30]. There is a wide range of values for mass flux at ignition dependent on material and environmental properties, however it is generally between $1 \text{ g}/(\text{m}^2\text{s})$ and $10 \text{ g}/(\text{m}^2\text{s})$ [29]. In the natural convection case of our general example, Fig. 11, the mass flux reached is much too low. It is not likely that any ignition events would be observed. However, in the induced flow cases, 2 m/s,

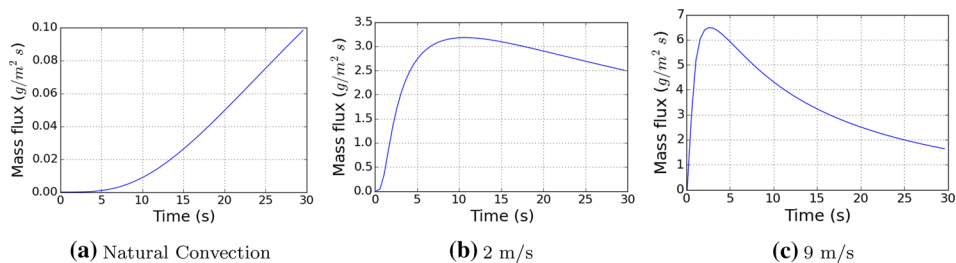


Figure 11. Mass loss rates over time for a large ember on a representative substrate for the experimental air flow conditions.

and 9 m/s, the mass fluxes peak very quickly and are much higher than that seen in the natural convection case. In these cases, earlier and more vigorous ignition is likely when a pilot of sufficient energy is present.

4. TGA Measurements for Parameterization

In order to compare the model to the results from the firebrand ignition tests, further parameterization of the materials was needed. Thermogravimetric analysis was performed on the materials. In order to fit the specifications of the TGA equipment, samples were approximately 5 mg. The samples were kept as close to the original form of the material as possible to avoid possible inconsistencies in the results due to differences in density, porosity, etc. Samples were heated at a rate of 20 K/min from 30°C to 800°C in an inert environment. Although a faster heating would better replicate the behavior during smoldering or flaming, 20 K/min is the maximum heating rate for our TGA instrument. The inert environment is used to represent the conditions for pyrolysis, which is the input to our model. Gani and Naruse noted that an inert environment is a better representation of a pyrolysis environment than an air environment [31]. Nassar et al. also used this reasoning in their work [32].

Figures 12 and 13 show representative curves for cellulosic and polymeric insulations. The FR and NFR cellulose and denim samples follow the typical degradation curves seen in cellulosic materials [33]. In the TGA tests, the effects of flame retardants are more obvious than in the firebrand ignition experiments. The NFR curves start to degrade after their FR counterparts, but have larger peaks and higher reaction rates. The individual reaction peaks are not as defined in the FR samples and are broader than the NFR samples. Additionally, as would be expected, the residual mass was larger for the FR cases. According to the manufacturer specifications, boric acid and ammonium sulfate were the flame retardants used in both denim and cellulose. Boric acid reduces the char oxidation and inhibits ignition through vapor phase dilution [34]. Similarly, ammonium sulfate encourages char formation through a dehydration mechanism [35]. The char formation promoted by the flame retardants reduces the overall mass loss and reactivity of the specimens.

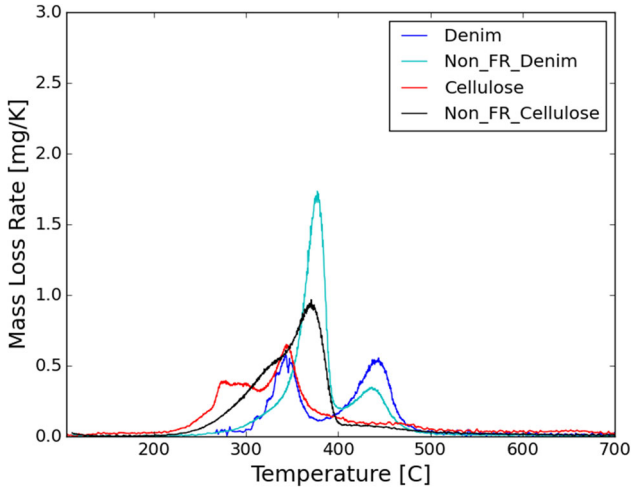


Figure 12. Mass loss rate curves for cellulosic materials at a 20 K/min heating rate.

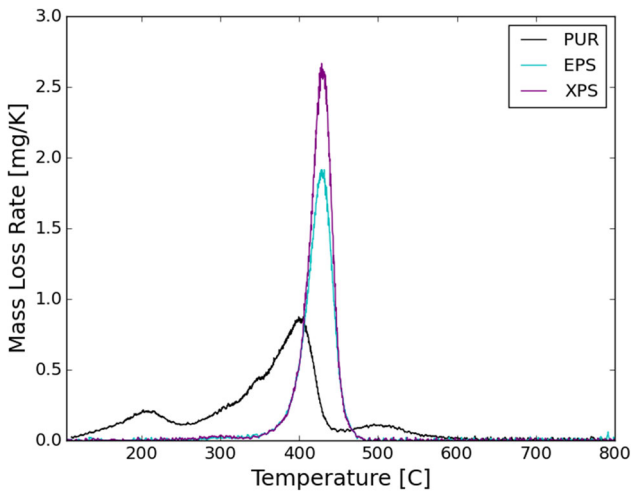


Figure 13. Mass loss rate curves for synthetic polymeric materials at a 20 K/min heating rate.

The XPS and EPS curves are very similar, which is to be expected as they are both forms of polystyrene. However the XPS has a higher residual mass fraction at the end of testing. In the firebrand ignition tests, XPS also had larger residual mass fractions compared to EPS. The PUR curve shows three peaks and bears some resemblance to the cellulosic mass loss curves with the largest peak at approximately 325°C and the final peak at about 500°C.

Table 3
Kinetic Parameters Derived from TGA Data Collected in a Nitrogen Environment with a 20 K/min Heating Rate

	E_a (J/mol)	A (s^{-1})
Denim	231,180	5.19 E 17
NFR denim	250,548	4.43 E 18
Cellulose	115,699	2.17 E 08
NFR cellulose	101,720	2.49 E 06
EPS	295,583	1.96 E 20
XPS	330,346	7.81 E 22
PUR	61,895	30,043

In addition to comparing the mass loss trends from the TGA tests, the kinetic parameters were determined using the method developed by Roberts [36]. The results for the first reaction are presented in Table 3. These kinetic parameters are the inputs to the model described in Sect. 3.2. It is important to note that the pre-exponential factor and the activation energies are generally coupled through kinetic-compensation. In general, activation energies and pre-exponential values for the same material can vary greatly depending on the methodology used to produce the parameters, but still produce similar mass loss trends.

5. Characterization Through Cone Calorimetry

Cone calorimetry can be used to determine many different characteristics of the material including heat release rate (HRR) and mass loss rates (MLR). Insulation samples were placed in double layer 10 cm \times 10 cm foil containers. Each material was tested at a variety of radiant heat fluxes—15 kW/m², 25 kW/m², and 35 kW/m². Tests were terminated 120 s after the sample flamed out or 300 s if no ignition occurred. For the cases with no ignition events, the peak MLR occurred prior to 300 s indicating that the sample would not ignite after 300 s.

The effects of radiant heating of the insulation samples varied depending on the material and the presence of flame retardants. At the highest incident heat flux tested (35 kW/m²), all samples burned. XPS and EPS samples left behind very little remaining residue. The residue was a thin char layer at some locations in the foil container. At the same incident heat flux, the NFR cellulose and denim left behind very little mass. The residual mass for these cases was a white ash structure. For the FR cellulose and denim, there was a significant mass of charred material post-test. This trend was also seen in the TGA experiments and is a result of the added flame retardants. For the PUR cases, there was more residual mass than the XPS and EPS, but less the FR cellulosic insulation cases. The remaining mass was a thin, brittle layer that covered the foil.

The TTIs for the different materials under an incident heat flux of 35 kW/m² can be seen in Table 4. At this flux there was fairly consistent ignition in all mate-

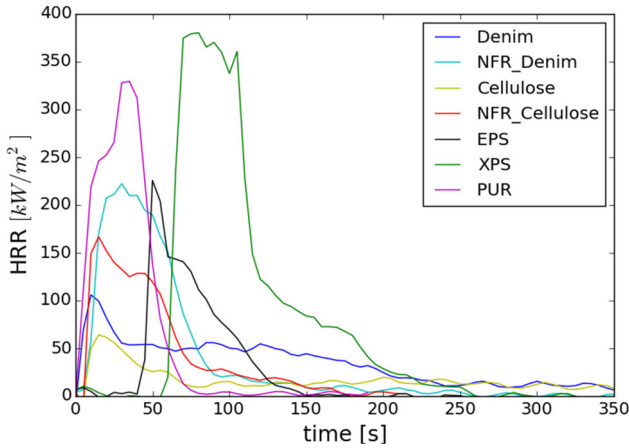


Figure 14. Heat release rates for all materials under a radiant heat flux of 35 kW/m².

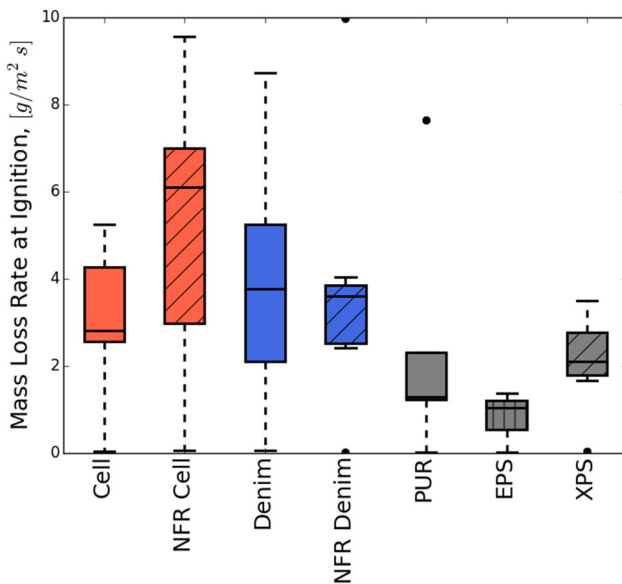


Figure 15. Tukey boxplots of the mass loss rates at ignition from at least a triplicate of tests run in the cone calorimeter.

rials. For the 15 kW/m² tests, XPS did not ignite. For 15 kW/m² and 25 kW/m² tests, EPS did not achieve ignition. EPS ignited in some, but not all tests at 35 kW/m² heat flux. Under all heat flux conditions, FR cellulose ignited for some tests, but not for others.

Table 4
Time to Ignition Results for the Insulation Materials Under an 35 kW/m² Applied Heat Flux in the Cone Calorimeter

Material	Time to ignition (s)
Denim	19.0 ± 24.4
NFR denim	15.2 ± 15.5
Cellulose	11.3 ± 11.9
NFR cellulose	Ignition in 4 out of 6 tests
EPS	5.5 ± 4.9
XPS	52.0 ± 34.3
PUR	Ignition in 4 out of 5 tests
	56.2 ± 11.8
	9.4 ± 10.3

Uncertainty values are calculated using a 95% confidence interval t-score

Table 5
Summary of Material Properties for the Different Insulation Materials Tested

	$k \left(\frac{\text{W}}{\text{mK}} \right)$	$c_p \left(\frac{\text{J}}{\text{kg K}} \right)$	$\rho \left(\frac{\text{kg}}{\text{m}^3} \right)$	$E_a \left(\frac{\text{J}}{\text{mol}} \right)$	A (s ⁻¹)	MLR $\left(\frac{\text{g}}{\text{m}^2 \text{s}} \right)$
Denim	0.038	1340	40	231,180	5.19 E 17	4.82
Cellulose	0.046	1300–1500	48	115,699	2.17 E 08	3.94
EPS	0.037	1500	20	295,583	1.96 E 20	1.29
XPS	0.022	1300–1500	21	330,346	7.81 E 22	2.77
PUR	0.025	1300	35	61,895	30,043	2.81

k and c_p come from manufacturer's data sheets ρ was measured. E_a and A were found using thermogravimetric analysis. Mass loss rate (MLR) at ignition was found via cone calorimetry

From the times to ignition presented in Table 4, the effects of flame retardants are more clear than in the firebrand ignition tests. The NFR samples had faster TTIs than their FR counterparts. Additionally in the case of cellulose and NFR cellulose, the non-flame retarded cellulose tests were more consistent. On average the cellulosic materials had lower TTIs compared to the polystyrenes, which have a lower melting point and higher vaporization point. Upon exposure to the radiant heat, EPS and XPS melt into a tar-like substance. A similar substance was observed in the firebrand ignition tests. The radiant heat must first melt the material leading to increased ignition times. TTIs for the polymeric materials tested in this study compare well with results from literature [37–39]. White et al. conducted experiments using cotton, which NFR denim is made of, and the results for TTI compare well [40]. Dlugogorski et al. and Dorez et al. studied mixed paper and cotton linter, respectively, which are analogous in composition to NFR cellulose [41, 42]. The TTI results from these two studies are comparable to the reported values in this work for NFR cellulose TTI. The FR denim and cellulose are unique materials, and the authors were unable to find any cone calorimetry

Table 6
Model Predicted Mass Fluxes for Various Materials Under the Three Different Air Flow Conditions

	Natural convection	2 m/s	9 m/s
Denim	$\ll 1 \text{ g/m}^2\text{s}$	$\gg 1 \text{ g/m}^2\text{s}$ (6 s)	$\gg 1 \text{ g/m}^2\text{s}$ (2 s)
Cellulose	$\ll 1 \text{ g/m}^2\text{s}$	$2.5 \text{ g/m}^2\text{s}$ (10 s)	$\gg 1 \text{ g/m}^2\text{s}$ (6 s)
EPS	$\ll 1 \text{ g/m}^2\text{s}$	$\sim 1 \text{ g/m}^2\text{s}$ (12 s)	$\gg 1 \text{ g/m}^2\text{s}$ (3 s)
XPS	$\ll 1 \text{ g/m}^2\text{s}$	$\sim 1 \text{ g/m}^2\text{s}$ (15 s)	$\gg 1 \text{ g/m}^2\text{s}$ (3 s)
PUR	$< 1 \text{ g/m}^2\text{s}$	$\sim 6 \text{ g/m}^2\text{s}$ (10 s)	$\sim 6 \text{ g/m}^2\text{s}$ (3 s)

The times the mass flux was taken at in the induced flow cases is presented in parentheses beneath the value

studies of these specific FR materials. For polymeric materials, the exposed surface to the heater recedes as the material melts, and the heat flux to the material decreases. The approximate reduction in heat flux for the 15 and 25 kW/m² cases were determined using a correlation between heat flux and distance from the cone heater developed by Shartel and Hull, and was estimated to be 3 kW/m² to 5 kW/m² [43]. Even accounting for this reduction in heat flux, the cellulosic materials are more likely to ignite compared to XPS and EPS. The uncertainty in measured TTI decreases with increasing heat flux, which is consistent with previous work [44]. At higher heat fluxes, the TTI is less sensitive to material inhomogeneity, which was also observed in the ember ignition tests.

The HRR data for the various materials at 35 kW/m² can be seen in Fig. 14. As with the time to ignition and the TGA tests, the effects of flame retardants are more obvious in the HRR curves than in the firebrand ignition experiments. In both denim and cellulose, the NFR samples have higher more narrow peaks compared to the FR samples. FR denim and cellulose have lower peak heat release rates, but they produce heat much longer than their NFR counterparts. In the cone calorimeter tests, the char formation from the flame retardants in the denim and cellulose is clearly visible. Char formation acts as a barrier to heat and mass transfer, which reduces, and in some cases, suppresses volatile production. Although XPS and EPS are both forms of polystyrene, XPS was found to have a higher average and peak HRR, which was also observed by An et al. [45].

The average MLR at ignition for the seven materials were found to be between 1 g/m²s and 6 g/m²s, with EPS having the smallest and NFR cellulose having the largest. Figure 15 shows the mass loss rate at ignition for the different insulation materials. Tukey boxplots are used to represent the distribution in the mass loss rates at ignition for each material. As previously discussed, ignition occurs when the amount of volatiles being produced is enough to form a combustible mixture that can be ignited by a spark. The MLR at ignition provides critical information

about the ability of a fuel to ignite and will peak near the TTI. The critical MLR is independent of incident heat flux as the MLR is temperature controlled. Similar critical MLR were found in literature [43].

6. Model Results Using Experimentally Determined Parameters

A summary of the material properties of the different insulation materials can be seen in Table 5. These properties come from manufacturer specifications, TGA experiments, and cone calorimetry. The kinetic parameters, E_a and A , are inputs to the model described in Sect. 3. The mass loss results for the flame retarded materials, both cellulosic and polymeric, can be seen in Table 6. These modeled mass fluxes are compared against the critical mass loss rates at ignition from Sect. 5 to determine whether or not the ignition criterion was met. In the natural convection cases, the peak mass loss rates were much lower than $1 \text{ g/m}^2\text{s}$. This indicates that ignition of the insulation materials from firebrands is very unlikely. In the induced flow cases, ignition becomes much more likely as the mass loss rates exceed $1 \text{ g/m}^2\text{s}$. The times in parentheses in the table indicate how long the firebrand had been interacting with the sample to reach the mass loss rate listed. The values listed for EPS and XPS under 2 m/s and 9 m/s air flow conditions indicate that ignition is possible. The model does not take into account the melting that occurs in EPS and XPS, so these results do not fully match the results that were observed experimentally in the firebrand ignition tests. It is more likely that melting and flash flaming would occur in these cases.

7. Conclusions

In an effort to explain the ignition process of substrates from firebrand deposition, an experimental setup and model were developed. The firebrand ignition experiments conducted on insulation materials showed that the tendency for ignition increases with increasing air flow rates. Additionally, consistent with existing literature, we found fragmented firebrand piles were more effective in igniting cellulosic materials compared to a single large firebrand. For synthetic polymers, such as EPS and XPS, we show that ember ignition is difficult because the embers melt through the material to regions where the absence of oxygen and cooling to substrate materials extinguishes them. These findings are in contrast to ignition tests conducted using radiant heating in a cone calorimeter. For cone testing, the synthetic polymers easily ignited. The ignition process in traditional lab scale experiments is significantly different than ignition by embers. A simple model for this process was developed. The model was parameterized using traditional laboratory scale tests—thermogravimetric analysis and cone calorimetry. The model predicted the same trends as the firebrand ignition experiments in regards to firebrand configuration and air flow rate effects. The model showed that the fragmented firebrand piles reach higher temperatures than the large firebrands, and firebrand

temperature increases with increasing air flow. Correspondingly, the model predicted reduced times for ignition with increased air flow, which was observed in the firebrand ignition experiments. For screening of insulative material ignition by wildfire firebrands, there is a clear need to develop testing protocols that accurately simulate the physical and chemical processes that actually occur in these systems. Publisher's Note Springer Nature remains neutral with regard to jurisdictional claims in published maps and institutional affiliations.

Acknowledgements

Funding was provided by the Department of Commerce through NIST (Grant no. 60NANB16D278) and by the Department of Interior through the Joint Fire Science Program under Project JFSP 15-1-04-4.

References

1. Martinuzzi S, Stewart SI, Helmers DP, Mockrin MH, Hammer RB, Radeloff VC (2015) The 2010 wildland-urban interface of the conterminous united states. Research Map NRS-8. US Department of Agriculture, Forest Service, Northern Research Station, Newtown Square, PA. 124 pp [includes pull-out map], 8:1–124
2. Caton SE, Hakes RSP, Gorham DJ, Zhou A, Gollner MJ (2017) Review of pathways for building fire spread in the wildland urban interface part i: exposure conditions. *Fire Technol* 53(2):429–473. <https://doi.org/10.1007/s10694-016-0589-z>
3. Manzello SL, Shields JR, Yang JC, Hayashi Y, Nii D (2007) On the use of a firebrand generator to investigate the ignition of structures in wildland–urban interface (WUI) fires. In: 11th International conference on fire science and engineering (INTERFLAM), pp 3–5
4. Long AJ, Randall CK (2004) Wildfire risk assessment guide for homeowners in the southern United States. School of Forest Resources and Conservation, University of Florida
5. Quarles SL, Valachovic Y, Nakamura GM, Nader GA, De Lasaux MJ (2010) Home survival in wildfire-prone areas: building materials and design considerations. ANR Publication, p 8393
6. Quarles S, Sindelar M et al (2011) Wildfire ignition resistant home design (WIRHD) program: full-scale testing and demonstration final report. Technical report, USDA Forest Service-Savannah River, New Ellenton, SC
7. Wang S, Huang X, Chen H, Liu N, Rein G (2015) Ignition of low-density expandable polystyrene foam by a hot particle. *Combust Flame* 162(11):4112–4118
8. Hadden RM, Scott S, Lautenberger C, Fernandez-Pello AC (2011) Ignition of combustible fuel beds by hot particles: an experimental and theoretical study. *Fire Technol* 47(2):341–355
9. Urban JL, Zak CD, Fernandez-Pello C (2018) Spot fire ignition of natural fuels by hot aluminum particles. *Fire Technol* 54(3):797–808
10. Wang S, Huang X, Chen H, Liu N (2017) Interaction between flaming and smouldering in hot-particle ignition of forest fuels and effects of moisture and wind. *Int J Wildland Fire* 26(1):71–81

11. Manzello SL, Cleary TG, Shields JR, Maranghides A, Mell W, Yang JC (2008) Experimental investigation of firebrands: generation and ignition of fuel beds. *Fire Saf J* 43(3):226–233
12. Ganteaume A, Lampin-Maillet C, Guijarro M, Hernando C, Jappiot M, Fonturbel T, Pérez-Gorostiaga P, Vega JA (2010) Spot fires: fuel bed flammability and capability of firebrands to ignite fuel beds. *Int J Wildland Fire* 18(8):951–969
13. Warey A (2018) Influence of thermal contact on heat transfer from glowing firebrands. *Case Stud Therm Eng* 12:301–311. <https://doi.org/10.1016/j.csite.2018.04.018>
14. Yin P, Liu N, Chen H, Lozano JS, Shan Y (2014) New correlation between ignition time and moisture content for pine needles attacked by firebrands. *Fire Technol* 50(1):79–91
15. Gol'dshleger UI, Pribytkova KV, Barzykin VV (1973) Ignition of a condensed explosive by a hot object of finite dimensions. *Combust Explos Shock Waves* 9(1):99–102
16. Jones JC (1993) Predictive calculations of the effect of an accidental heat source on a bed of forest litter. *J Fire Sci* 11(1):80–86
17. Jones JC (1995) Improved calculations concerning the ignition of forest litter by hot particle ingress. *J Fire Sci* 13(5):350–356
18. Babrauskas V (2003) *Ignition handbook*. Fire Science Publishers, Issaquah, WA ISBN:0972811133
19. Lautenberger C, Fernandez-Pello AC (2009) Spotting ignition of fuel beds by firebrands. *WIT Trans Model Simul* 48:603–612
20. Manzello SL, Maranghides A, Shields JR, Mell WE, Hayashi Y, Nii D (2007) Measurement of firebrand production and heat release rate (HRR) from burning Korean pine trees. *Fire Saf Sci* 7:108–108
21. El Houssami M, Mueller E, Filkov A, Thomas JC, Skowronski N, Gallagher MR, Clark K, Kremens R, Simeoni A (2016) Experimental procedures characterising firebrand generation in wildland fires. *Fire Technol* 52(3):731–751
22. International Code Council (2018) *International residential code for one-and two-family dwellings*. International Code Council
23. Damant GH, Williams SS, McCormack JA (1983) The role of fabric in the cigarette ignition of upholstered furniture. *J Fire Sci* 1(5):309–321
24. Zak CD (2015) *The effect of particle properties on hot particle spot fire ignition*. University of California, Berkeley
25. Persoons T, McGuinn A, Murray DB (2011) A general correlation for the stagnation point Nusselt number of an axisymmetric impinging synthetic jet. *Int J Heat Mass Transf* 54(17):3900–3908. <https://doi.org/10.1016/j.ijheatmasstransfer.2011.04.037>
26. Bergman TL, Incropera FP, DeWitt DP, Lavine AS (2011) *Fundamentals of heat and mass transfer*. Wiley, New York
27. Drysdale D (2011) *An introduction to fire dynamics*. Wiley, New York
28. Bamford CH, Crank J, Malan DH (1946) The combustion of wood. Part I. In: *Mathematical proceedings of the Cambridge Philosophical Society*, vol 42, pp 166–182. Cambridge University Press
29. Drysdale DD, Thomson HE (1989) Flammability of plastics ii: critical mass flux at the firepoint. *Fire Saf J* 14(3):179–188. [https://doi.org/10.1016/0379-7112\(89\)90071-4](https://doi.org/10.1016/0379-7112(89)90071-4)
30. Tsai T-H, Li M-J, Shih I-Y, Jih R, Wong S-C (2001) Experimental and numerical study of autoignition and pilot ignition of PMMA plates in a cone calorimeter. *Combust Flame* 124(3):466–480
31. Gani A, Naruse I (2007) Effect of cellulose and lignin content on pyrolysis and combustion characteristics for several types of biomass. *Renew Energy* 32(4):649–661. <https://doi.org/10.1016/j.renene.2006.02.017>

32. Nassar MM, Ashour EA, Wahid SS (1996) Thermal characteristics of bagasse. *J Appl Polym Sci* 61(6):885–890
33. Munir S, Daood SS, Nimmo W, Cunliffe AM, Gibbs BM (2009) Thermal analysis and devolatilization kinetics of cotton stalk, sugar cane bagasse and shea meal under nitrogen and air atmospheres. *Bioresour Technol* 100(3):1413–1418
34. Wang Q, Li J, Winandy JE (2004) Chemical mechanism of fire retardance of boric acid on wood. *Wood Sci Technol* 38(5):375–389
35. Mostashari SM, Mostashari SZ (2008) Combustion pathway of cotton fabrics treated by ammonium sulfate as a flame-retardant studied by TG. *J Therm Anal Calorim* 91(2):437–441
36. Roberts BC (2017) Fire safety in sustainable buildings: status, options, alternatives. The University of California at Austin, Austin
37. Bakhtiyari S, Taghi-Akbari L, Barikani M (2010) The effective parameters for reaction-to-fire properties of expanded polystyrene foams in bench scale. *Iran Polym J* 19:27–37
38. Irvine DJ, McCluskey JA, Robinson IM (2000) Fire hazards and some common polymers. *Polym Degrad Stab* 67(3):383–396
39. Usta N (2012) Investigation of fire behavior of rigid polyurethane foams containing fly ash and intumescent flame retardant by using a cone calorimeter. *J Appl Polym Sci* 124(4):3372–3382. <https://doi.org/10.1002/app.35352>
40. White RH, Nam S, Parikh DV (2013) Cone calorimeter evaluation of two flame retardant cotton fabrics. *Fire Mater* 37(1):46–57
41. Dlugogorski BZ, Hirunpraditkoon S, Kennedy EM (2014) Ignition temperature and surface emissivity of heterogeneous loosely packed materials from pyrometric measurements. *Fire Saf Sci* 11:262–275
42. Dorez G, Ferry L, Sonnier R, Taguet A, Lopez-Cuesta J-M (2014) Effect of cellulose, hemicellulose and lignin contents on pyrolysis and combustion of natural fibers. *J Anal Appl Pyrol* 107:323–331. <https://doi.org/10.1016/j.jaap.2014.03.017>
43. ScharTEL B, Hull TR (2007) Development of fire-retarded materials—interpretation of cone calorimeter data. *Fire Mater* 31(5):327–354
44. ScharTEL B, Bartholmai M, Knoll U (2005) Some comments on the use of cone calorimeter data. *Polym Degrad Stab* 88(3):540–547
45. An W, Jiang L, Sun J, Liew KM (2015) Correlation analysis of sample thickness, heat flux, and cone calorimetry test data of polystyrene foam. *J Therm Anal Calorim* 119(1):229–238